Spin-dependent thermal transport perpendicular to the planes of Co/Cu multilayers

Johannes Kimling, R. B. Wilson, Karsten Rott, Judith Kimling, Günter Reiss, and David G. Cahill

Phys. Rev. B **91**, 144405 — Published 7 April 2015

DOI: 10.1103/PhysRevB.91.144405

Spin-dependent thermal transport perpendicular to the planes of Co/Cu multilayers

Johannes Kimling,[1,*] R. B. Wilson,[1] Karsten Rott,[2]
Judith Kimling,[1] Günter Reiss,[2] and David G. Cahill[1]

[1]*Department of Materials Science and Engineering and Materials Research Laboratory, University of Illinois, Urbana, Illinois 61801, USA*

[2]*Fakultät fur Physik, Universität Bielefeld, 33501 Bielefeld, Germany*

(Dated: March 19, 2015)

Abstract

We report measurements of the cross-plane thermal conductivity of periodic Co/Cu multilayers using time-domain thermoreflectance. The cross-plane thermal conductivity increases from ~ 18 W m^{-1} K^{-1} at remanence to ~ 32 W m^{-1} K^{-1} at saturation fields. This giant magnetothermal resistance (GMTR) effect is consistent with predictions based on the Wiedemann-Franz law. We discuss the role of a spin-dependent temperature, known as spin heat accumulation, in GMTR experiments and develop a three-temperature model capable of predicting the time-evolution of the temperatures of majority-spin electrons, minority-spin electrons, and phonons subsequent to pulsed laser heating.

PACS numbers:

I. INTRODUCTION

The electrical conductivity through periodic Co/Cu multilayers can show changes up to 50% upon application of a magnetic field[1,2]. This giant magnetoresistance (GMR) has a thermal analog observed in the CIP geometry (heat-current-in-plane) that is known as giant magnetothermal resistance (GMTR)[3,4]. More recently, nanoscale thermal transport from a ferromagnetic metal into a nonmagnetic conductor has attracted interest in the field of spin caloritronics[5] due to the possibility of generating a spin-dependent temperature near the interface[6–9]. The concept of different effective temperatures $T_\uparrow$ and $T_\downarrow$ for majority- and minority-spin electrons is known as spin heat accumulation (SHA). SHA plays a key role in the theory of GMTR in the CPP geometry (heat-current-perpendicular-to-plane), similar to spin accumulation in the theory of CPP-GMR[10,11]. Therefore, the observation of CPP-GMTR in spin valves composed of two ferrmagnetic metals separated by a normal metal spacer has been interpreted as a proof of the existence of SHA[7,9]. Considerably larger effects are expected in periodic magnetic multilayers composed of a large number of stacked spin valves.

Here, we focus on thermal transport through periodic Co/Cu multilayers in the hitherto unexplored geometry perpendicular to the sample plane. In Sec. II, we facilitate understanding of CPP-GMTR and SHA by discussing spin-dependent thermal diffusion in steady-state. We use a three-temperature model of majority-spin electrons, minority-spin electrons, and phonons to derive spin heat relaxation lengths in Co and in Cu. Based on these results, we apply the Wiedemann-Franz law to predict thermal conductivities and CPP-GMTR of our samples. In Sec. III, we present experimental measurements of cross-plane thermal conductivity and CPP-GMTR of Co/Cu multilayers. In Sec. IV, we first discuss the ontological status of SHA. Then, we use the three-temperature model to predict the time evolution of SHA in a Co/Cu multilayer subsequent to pulsed laser heating as conjectured in the experiments of Sec. III.

II. THEORY

A. Spin heat accumulation in steady-state

In a ferromagnetic metal (F) like Co, heat transport is dominated by electrons. Based on the Wiedemann-Franz (W-F) law, the thermal conductivity Λ of a ferromagnet is spin-polarized. In Co, $\Lambda_\uparrow$ of majority-spin electrons is larger than $\Lambda_\downarrow$ of minority-spin electrons. In a normal metal (N) like Cu, both thermal conductivities are equal. As a consequence of the disparate thermal transport properties on both sides of a F/N interface, thermal transport from F to N results in $T_\uparrow \neq T_\downarrow$ near the interface.

Diffusion of SHA in steady-state has been described using the thermal equivalent of the diffusion equation of spin accumulation[7,11,12],

$$\frac{\partial^2(T_\uparrow - T_\downarrow)}{\partial z^2} = \frac{T_\uparrow - T_\downarrow}{l_\mathrm{q}^2}. \tag{1}$$

The spin heat relaxation length l_q is the thermal equivalent of the spin-diffusion length l_sf[11]. According to Eq. 1, SHA at a F/N interface decays exponentionally with distance from the interface. In Appendix A, we solve Eq. 1 for a F/N bilayer and for a periodic F/N multilayer assuming uniform heat current perpendicular to the interface. For simplicity, we consider only spin-dependent scattering in the bulk and assume transparent interfaces. The solutions $T_\uparrow(z)$ and $T_\downarrow(z)$ across a F/N bilayer are plotted in Fig. 1 (a) together with the spin-averaged temperature T that is discontinuous at the interface. As indicated in Fig. 1 (a), SHA at a F/N interface rises with increasing spin heat relaxation lengths l_qF and l_qN, and increasing spin-asymmetry coefficient $\beta = (\Lambda_\uparrow - \Lambda_\downarrow)/(\Lambda_\uparrow + \Lambda_\downarrow)$. Adding a spin-dependent interface thermal conductance with positive spin-asymmetry coefficient would contribute to SHA in the normal metal. For thermal transport in the reversed direction, the sign of SHA changes.

In a F/N multilayer, the heat flux successively traverses F/N and N/F interfaces. We are interested in two magnetic configurations of the multilayer: the antiparallel (AP) configuration (magnetization vectors of adjacent F layers are aligned antiparallel) and the parallel (P) configuration (magnetization vectors are parallel). As discussed above, SHA near a F/N interface changes sign when reversing the direction of the heat current. This means that in the P configuration, superposition of SHA at successive interfaces reduces the amount of SHA at each interface, provided that l_qN is comparable to the N-layer thickness or larger. The change of sign of SHA within the N layers can be removed by switching the magnetic

configuration from P to AP. In the AP configuration, superposition of SHA increases the amount of SHA in each N layer. The sign of SHA alternates between successive N layers. Note that in AP configuration, the spin character ($\uparrow$ or $\downarrow$) of the two electron heat channels alternates through successive F layers. Therefore, we use '+' and '−' to distinguish the two electron heat channels in the AP configuration.

The solutions $T_+(z)$ and $T_-(z)$ across a periodic F/N multilayer in AP and P configuration are plotted in Fig. 1 (b) and (c), together with the spin-averaged temperature T that is discontinuous at the interfaces. The model assumes $l_{\mathrm{qF}} = 5h$ and $l_{\mathrm{qN}} = 50h$, where $2h$ is the thickness of one layer. Since the temperature drop across a bilayer is proportional to the thermal resistance of the bilayer, the difference in the temperature drop for the two magnetic configurations reveals the CPP-GMTR effect. As indicated in Fig. 1 (b) in the limit $\{l_{\mathrm{qF}}, l_{\mathrm{qN}}\} \gg h$, the amount of SHA and the size of CPP-GMTR are proportional to β. In the limit, $l_{\mathrm{qN}} \ll h$, SHA at successive interfaces are decoupled and CPP-GMTR vanishes.

B. Time-dependent three-temperature model

The steady-state diffusion equation of SHA, Eq. (1), does not consider energy transfer between electrons and phonons explicitly. As discussed in Sec. III, we use a pump-and-probe experiment that measures the temperature decay of the sample surface subsequent to pulsed laser heating. To describe the dynamic of the spin-dependent electron temperature, we use a three-temperature thermal diffusion model that considers $\uparrow$ electrons, $\downarrow$ electrons, and phonons as weakly coupled thermodynamic reservoirs. Weakly coupled means that thermalization occurs much faster within a reservoir than between the reservoirs, as implicated by the phenomenon of GMTR. The electrons dominate heat conduction and the phonons dominate the heat capacity. The three-temperature model reads

$$C_\uparrow \frac{dT_\uparrow}{dt} = g_{\uparrow \mathrm{p}}(T_\mathrm{p} - T_\uparrow) + g_{\uparrow\downarrow}(T_\downarrow - T_\uparrow) + \Lambda_\uparrow \frac{d^2 T_\uparrow}{dz^2}, \tag{2}$$

$$C_\mathrm{p} \frac{dT_\mathrm{p}}{dt} = g_{\uparrow \mathrm{p}}(T_\uparrow - T_\mathrm{p}) + g_{\downarrow \mathrm{p}}(T_\downarrow - T_\mathrm{p}) + \Lambda_\mathrm{p} \frac{d^2 T_\mathrm{p}}{dz^2}, \tag{3}$$

$$C_\downarrow \frac{dT_\downarrow}{dt} = g_{\downarrow \mathrm{p}}(T_\mathrm{p} - T_\downarrow) + g_{\uparrow\downarrow}(T_\uparrow - T_\downarrow) + \Lambda_\downarrow \frac{d^2 T_\downarrow}{dz^2}, \tag{4}$$

where C denotes volumetric heat capacity, Λ denotes thermal conductivity, and g denotes coupling parameter between the reservoirs; the subscript p refers to the thermodynamic

reservoir of phonons. We use the three-temperature model to express the spin heat relaxation length in terms of coupling parameters and thermal conductivities, which allows for estimation of spin heat relaxation lengths in Co and in Cu.

Due to the coupling between the electron channels and the phonons, the diffusion equation of SHA, Eq. (1), cannot be derived in general from the three-temperature model. At room temperature, electron-phonon scattering dominates the spin heat relaxation length[7], i.e., $g_{\mathrm{ep}} \gg g_{\uparrow\downarrow}$. Neglecting direct coupling between $\uparrow$ and $\downarrow$ electrons, the steady-state three-temperature model ($dT/dt = 0$) implies a double-exponential decay of SHA with the two relaxation lengths,

$$l_{\mathrm{q1}} = \sqrt{\frac{\Lambda_\uparrow}{g_{\uparrow\mathrm{p}}}}, \quad l_{\mathrm{q2}} = \sqrt{\frac{\Lambda_\downarrow}{g_{\downarrow\mathrm{p}}}}. \tag{5}$$

However, in a normal metal, $g_{\uparrow\mathrm{p}} = g_{\downarrow\mathrm{p}}$ and $\Lambda_\uparrow = \Lambda_\downarrow$. Hence, the steady-state Eq. (1) can be derived by subtracting Eq. (4) from Eq. (2). The resulting spin heat relaxation length in the normal metal reads

$$l_{\mathrm{qN}} = \sqrt{\frac{\Lambda_\uparrow}{g_{\uparrow\mathrm{p}} + 2g_{\uparrow\downarrow}}} \approx \sqrt{\frac{\Lambda_\uparrow}{g_{\uparrow\mathrm{p}}}}, \tag{6}$$

where the approximation is valid at room temperature (see discussion above).

We use Eqs. (5) and (6) to estimate the spin heat relaxation lengths of Co and of Cu. We estimate the thermal conductivity of Co, $\Lambda_{\mathrm{Co}} \approx 58$ W m^{-1} K^{-1}, and of Cu, $\Lambda_{\mathrm{Cu}} \approx 170$ W m^{-1} K^{-1}, using electrical resistivities measured on 100-nm-thick films and the W-F law. We assume a spin-asymmetry coefficient of $\beta = 0.46$, which equals the spin-asymmetry coefficient of the electrical conductivity measured at liquid Helium temperatures[13]. Since β is expected to decrease slightly with temperature, considering the low-temperature value of β yields a lower limit for l_{q2}. The electron-phonon coupling parameter of Cu, $g_{\mathrm{ep}} \approx 7.5 \times 10^{16}$ W m^{-3} K^{-1}, has been determined experimentally in Ref. 14. We estimate the electron-phonon coupling parameter of Co with $g_{\mathrm{ep}} \approx 4.5 \times 10^{17}$ W m^{-3} K^{-1} of Pt determined experimentally in Ref. 15. To estimate the spin-asymmetry of g_{ep} in Co, we use the ratio of the dimensionless electron-phonon coupling constants, $\lambda^\uparrow/\lambda^\downarrow = 0.16$, determined in Ref. 16 using *Ab initio* calculations. We finally obtain $l_{\mathrm{q1}} \approx 27$ nm, $l_{\mathrm{q2}} \approx 7$ nm, and $l_{\mathrm{qN}} \approx 34$ nm.

C. Wiedemann-Franz law

While $l_{\rm sf}$ is limited by spin-flip scattering, $l_{\rm q}$ is limited by spin-flip scattering and electron-phonon scattering[6]. At high temperatures, relaxation of SHA via electron-phonon scattering dominates, i.e., $l_{\rm q} < l_{\rm sf}$. Since spin-conserving electron-phonon scattering does not affect spin accumulation, CPP-GMTR could be smaller than CPP-GMR, e.g., if $l_{\rm qN} < h < l_{\rm sf}$, resulting in a magnetic-field dependent Lorenz number[6].

In typical Co/Cu multilayers, the thickness of the individual layers is of the order of 1 nm. In Sec. III, we present experimental results on Co(3nm)/Cu(1nm) multilayers. Since the Co and Cu layer thicknesses are well below the spin heat relaxation lengths estimated in Sec. II B, we can use the W-F law to predict the thermal conductivity of a Co(3nm)/Cu(1nm) multilayer in AP and P configuration.

The cross-plane electrical resistivity of Co/Cu multilayers has been measured at liquid helium temperatures, where the dominating resistance of contact leads can be circumvented by using superconducting strips[13]. Using a two-current series resistor (2CSR) model valid for layer thicknesses well below the spin-diffusion lengths[11], Bass *et al.*[13] determined the spin-asymmetry coefficients $\beta = (\sigma_\uparrow - \sigma_\downarrow)/(\sigma_\uparrow + \sigma_\downarrow) = 0.46 \pm 0.05$ and $\gamma = (AR_\downarrow - AR_\uparrow)/(AR_\uparrow + AR\downarrow) = 0.77 \pm 0.04$ of the electrical conductance σ of Co and the resistance area product AR of a Co/Cu interface. They further determined a renormalized resistance area product of a Co/Cu interface of $AR^* = AR/(1-\gamma^2) = 0.5$ fΩm^2. We measured the electrical resistivity $\rho_{\rm Co} = 15.2$ $\mu\Omega$ cm and $\rho_{\rm Cu} = 4.25$ $\mu\Omega$ cm at room temperature on 100-nm-thick sputtered Co and Cu films. The resistivity of similarily sputtered films of the same material typically varies within approximately 10%. Assuming that spin-asymmetry coefficients and interface resistance do not change significantly with temperature, the 2CSR model of a Co(3nm)/Cu(1nm) multilayer predicts electrical resistivities of

$$\rho_{\rm AP} = \frac{h_{\rm Co}\rho^*_{\rm Co} + h_{\rm Cu}\rho_{\rm Cu} + AR^*}{h_{\rm Co} + h_{\rm Cu}} = (41 \pm 2)\ \mu\Omega{\rm cm}, \tag{7}$$

$$\rho_{\rm P} = \rho_{\rm AP} - \frac{(h_{\rm Co}\beta\rho^*_{\rm Co} + \gamma AR^*)^2}{(h_{\rm Co} + h_{\rm Cu})^2\rho_{\rm AP}} = (24 \pm 2)\ \mu\Omega{\rm cm}, \tag{8}$$

where $2h_{\rm Co}$ and $2h_{\rm Cu}$ are the thicknesses of the Co and Cu layers, and $\rho^* = \rho/(1-\beta^2)$ is a renormalized resistivity. Hence, using the W-F law, we expect to measure thermal conductivities of $\Lambda_{\rm AP} \approx (18 \pm 1)$ W m^{-1} K^{-1} and $\Lambda_{\rm P} \approx (30 \pm 2)$ W m^{-1} K^{-1} corresponding to a CPP-GMTR ratio of $(\Lambda_{\rm P} - \Lambda_{\rm AP})/\Lambda_{\rm P} \approx (41 \pm 5)\%$.

III. EXPERIMENT

A. Time-domain thermoreflectance setup

TDTR is an optical pump and probe technique: the sample surface is heated using sub-ps laser pulses and temperature changes of the sample are detected via changes in the intensity of reflected sub-ps probe laser pulses[17–19]. TDTR measurements can be used to determine thermal properties of materials and to study nanoscale thermal transport[20]. A sketch of our TDTR setup is depicted in Fig. 2. We use a Ti:sapphire laser oscillator that produces a train of sub-ps optical pulses at a repetition rate of 80 MHz. The laser oscillator is adjusted to output a center wavelength of 783 nm and a full width at half maximum (FWHM) bandwidth of 12 nm. The laser beam is split into a pump beam and a probe beam. To suppress pump laser light from leaking into the detector, we combine two approaches: (i) separation of the polarization of pump and probe light using polarizing beam splitters; (ii) separation of the spectrum of pump and probe light by approximately 8 nm using ultasteep edge filters. The optical path of the pump beam includes an electro-optic modulator chopping the pump beam at 10 MHz, followed by an optical delay line. The optical path of the probe beam includes a mechanical chopper modulating the probe beam at 200 Hz to facilitate the removal of coherent pick-up by the RF Lock-in Amplifier. Pump and probe light is focused on the sample by a single microscope objective. The $1/e^2$ intensity radius of correlated pump and probe pulses at the sample is 6.1 μm; the FWHM of the temporal correlation of pump and probe pulses at the sample is 1.2 ps. Most of the temporal broadening is coming from the ultrasteep long-pass filter in the pump path.

The maximum temperature excursion created by each pump optical pulse is $\sim$ 10 K. Since this is a small fraction of absolute temperature, the thermal response of the sample is linear in both the pump and probe powers allowing for a frequency domain description of the signals (compare Ref. 18). In the frequency domain, the incident probe beam can be represented by a frequency comb of delta functions separated by 80 MHz, while the modulated incident pump beam, and thus the thermal response of the sample, includes additional side bands at 10, 70, 90, 150, 170 MHz, etc. The reflected probe signal can be represented as a convolution of the frequency spectra of the incident probe beam and the thermal response of the sample. The components of the reflected probe signal at $\pm$ 10 MHz

are extracted by an RF Lock-in Amplifier after conversion into an electrical signal using a photodiode. The double modulation approach employed includes an audio-frequency Lock-in amplifier for recording the output of the RF Lock-in Amplifier at 200 Hz.

B. Time-domain thermoreflectance analysis

The TDTR signal is recorded as a function of time delay between pump and probe pulses. The time delay is varied between -20 ps and 4 ns. Since the diameter of the pump beam is much larger than the thermal diffusion distance at maximum time delay, thermal transport on the short time-scales between pump and probe pulses is predominately one-dimensional. The in-phase component V_{in} of the measurement voltage oscillates in-phase with the 10 MHz modulation of the pump beam and can be interpreted as the time-domain response of the sample to pulsed heating. The out-of-phase component V_{out} of the measurement voltage does not change significantly with time delay[18]. We analyze the ratio $-V_{\text{in}}/V_{\text{out}}$, which is independent of laser intensities, sample absorptivity, and thermoreflectance coefficient, and insensitive to accidental nonconcentric alignment of the pump and probe beams[21,22]. Moreover, analyzing the ratio $-V_{\text{in}}/V_{\text{out}}$ can approximately correct for changes in the diameter of the pump beam with time delay.

Thermal transport properties of the sample are determined by adjusting free parameters in a heat diffusion model to obtain the best fit between the predicted and measured thermal response of the sample[18]. While a three-temperature model is required to explain why the thermal conductivity of the Co/Cu multilayer changes upon application of a magnetic field, determination of the effective thermal conductivity as a function of magnetic field can be achieved using a one-channel heat diffusion model. We assume that the initial temperature profile is proportional to the absorption profile. To account for the initial temperature distribution, we use a bidirectional heat diffusion model and make use of the superposition principle. The bidirectional model splits the transducer layer into two layers. At the artificial interface, a heat flux boundary condition is used to model the absorption of laser energy. We solve the model for varying depths of the artificial interface. Superposition of the resulting thermal responses weighted by the normalized optical absorption profile yields the thermal response of the sample. An example of this approach are shown in Fig. 7 (a) in Appendix B.

Determining the intitial temperature profile from the optical absorption profile can be

problematic in metals with weak electron-phonon coupling, such as Cu, because electronic heat conduction during thermalization of electrons and phonons can alter the initial temperature profile in the nanometer length-scale[23]. However, as demonstrated in Appendix B, the thermal response of our samples is insensitive to the initial temperature profile for time delays longer than ~ 200 ps. Analyzing TDTR data in the time delay range between 200 ps and 4 ns, we can further assume that the temperature variation within the optical penetration depth is small compared to the average temperature excursion [compare Fig. 7 (b) in Appendix B].

C. Experimental results

We measured the cross-plane thermal conductivity of Co(3nm)/Cu(1nm) multilayers using time-domain thermoreflectance (TDTR) as described in Secs. III A and III B. The Co(3nm)/Cu(1nm) multilayers were deposited on MgO substrates using magnetron-sputtering. Sample I is composed of 39 Co/Cu bilayers with a 2-nm-thin Ru layer on top. A scematic of Sample I is depicted in Fig. 3 (a). Sample II is composed of the same layer stack as Sample I, only the Ru layer is 60 nm thick. Sample III is composed of a 25-nm-thin Co(3nm)/Cu(1nm) multilayer covered with a 2-nm-thin Ru layer. Exchange coupling between the ferromagnetic Co layers results in an antiparallel magnetic ground state. By applying magnetic fields, the magnetization vectors of the Co layers can be aligned parallel.

We used a reference sample composed of a 60-nm-thick Ru layer sputtered directly on MgO to determine the thermal conductivity of the MgO substrates from TDTR measurements and the thermal conductivity of Ru from four-probe sheet resistance measurements and the Wiedemann-Franz law.

TDTR measurements on Sample I and Sample II clearly resolve the CPP-GMTR effect. Figure 3 (b) depicts TDTR data measured on Sample I at zero applied field (AP configuration) and in an applied in-plane field of $\mu_0 H = 400$ mT (P configuration). The TDTR ratio $-V_{\rm in}/V_{\rm out}$ of in-phase and out-of-phase signals is plotted as a function of time delay t and mimics the thermal response of the sample. Due to CPP-GMTR, the measurements show a faster temperature decay for the P configuration. Analysis of TDTR data from Sample I yields CPP thermal conductivities of $\Lambda_{\rm AP} = (18 \pm 2)$ W m^{-1} K^{-1} and $\Lambda_{\rm P} = (32 \pm 3)$ W m^{-1} K^{-1}, corresponding to a CPP-GMTR ratio of $(\Lambda_{\rm P} - \Lambda_{\rm AP})/\Lambda_{\rm P} = 0.44 \pm 0.08$.

The systematic error includes uncertainties in the thermal conductivity of the MgO substrate and in the thickness of the Co/Cu multilayer. The best fit curves are shown as solid lines in Fig. 3 (b). The parameter set of the heat diffusion model of Sample I is listed in Table I.

For Sample II, due to the increased sample thickness, a part of the sensitivity to the thermal conductivity of the Co/Cu multilayer is shifted to the out-of-phase signal. Therefore, the corresponding TDTR ratios in AP and P configuration cross at $\sim$ 200 ps [compare Fig. 3 (c)], although the in-phase signals differ only for time delays longer than $\sim$ 100 ps. We obtain thermal conductivities of $\Lambda_{\mathrm{AP}} = (17 \pm 1)$ W m^{-1} K^{-1} and $\Lambda_{\mathrm{P}} = (28 \pm 5)$ W m^{-1} K^{-1}, corresponding to a CPP-GMTR ratio of $(\Lambda_{\mathrm{P}} - \Lambda_{\mathrm{AP}})/\Lambda_{\mathrm{P}} = 0.39 \pm 11$. Compared to Sample I, the systematic error is larger due to additional uncertainties in the thermal conductivity of the Ru layer. The parameter set of the heat diffusion model of Sample II is listed in Table II.

TDTR measurements on Sample III are insensitive to thermal transport through the Co/Cu multilayer, because the thickness of the sample is comparable to the optical penetration depth. As shown in Fig. 3 (d), we obtained identical in-phase signals for both magnetic configurations. This shows that the influence of a giant magnetorefractive effect (MRE) is negligible. MRE describes changes in the refractive index of a magnetic multilayer due to changes in the magnetic configuration, which can become significant at infrared wavelengths longer than $\sim$ 5 μm[24]. Moreover, the TDTR ratio is insensitive to the absorption in the sample and thus insensitive to MRE.

The sizeable CPP-GMTR observed for Sample I and Sample II and the magnitude of the results are in very good agreement with the predictions from the W-F law in Sec. II C, where we used spin-asymmetry coefficients of the electrical conductivity of Co and of the electrical interface conductance from Ref. 13 measured at liquid Helium temperatures. We note that spin asymmetry coefficients of Co/Cu multilayers have only been determined at low temperatures, where the dominating resistance of contact leads can be circumvented by using superconducting strips[13]. The size of CPP-GMTR observed in this work indicates that the spin asymmetry parameters do not change significantly with temperature.

Furthermore, we measured the in-plane electrical resistivity of Sample I as a function of applied magnetic field using van der Pauw measurements. In Fig. 4, we compare the resulting CIP-GMR curve with the magnetic-field dependence of the cross-plane thermal conductivity determined from TDTR measurements at constant time delay. The CIP-GMR

shows similar magnetic-field dependence as the CPP-GMTR. However, the CIP-GMR ratio of $(\rho_{\mathrm{AP}} - \rho_{\mathrm{P}})/\rho_{\mathrm{AP}} = 0.34$ is clearly smaller than the CPP-GMTR ratio. To address the anisotropy of electrical and thermal transport in Co/Cu multilayers in more detail, we recap results from a prior work, where we studied CIP-GMTR in periodic Co(3nm)/Cu(1nm) multilayers[25]. We obtained similar in-plane electrical resistivities of $\widetilde{\rho}_{\mathrm{AP}} \approx 19 \times 10^{-8}$ and $\widetilde{\rho}_{\mathrm{P}} \approx 27 \times 10^{-8}\ \Omega$ m, which confirms the comparability of the two studies. Both CIP-GMR and CIP-GMTR ratios determined in the prior study are approximately 30%, well below the CPP-GMTR ratio of $(44 \pm 8)\%$ of the present study. In the CIP geometry, the probability of electrons to transport heat through successive Co layers is reduced in comparison to the CPP geometry. Shunting heat currents parallel to the plane of the layers increase the thermal conductivity in the AP configuration thereby reducing the CIP-GMTR ratio.

IV. DISCUSSION

In Sec. II, we demonstrated that the steady-state theory of CPP-GMTR in F/N multilayers predicts SHA in the AP configuration of the multilayer. As stated in Sec. I, the observation of CPP-GMTR in spin valves has been interpreted as a proof of the existence of SHA[7,9]. We believe that this conclusion is too strong. Both SHA and CPP-GMTR are predictions derived from a spin-dependent scattering theory. While the prediction of CPP-GMTR has been verified in spin valves[7] and with this work in periodic Co/Cu multilayers, the prediction of SHA still needs to be verified experimentally. This could be accomplished, e.g., using spin-selective thermometers[6]. Observation of CPP-GMTR is consistent with the concept SHA, but does not verify the prediction of SHA.

In Sec. III, we determined the thermal conductivity of Co/Cu multilayers from TDTR measurements using a one-channel heat diffusion model. In the following, we discuss the simulation of the TDTR experiments on Sample I using the three-temperature model discussed in Sec. II B. We extend Eqs. (2) through (4) to a multilayer model and consider a spin-dependent interface thermal conductance for the electron heat channels at the Co/Cu interfaces. Note that in the AP configuration the spin character ($\uparrow$ or $\downarrow$) of the two electron heat channels is not unique, but alternates through successive Co layers. The parameters used for modeling Sample I are listed in Table IV and discussed in Appendix C. Of significance in the following discussion are only the electron-phonon coupling parameters defined

in Sec. II B, and the spin-dependent thermal conductance per unit area of a Co/Cu interface determined from the spin-dependent interface resistance discussed in Sec. II C and the W-F law[26]. We assume that laser energy is transfered to the two electron reservoirs with equal rates. In accordance with the TDTR experiments, we consider a heat pulse with an average fluence of 0.85 J m^{-2}, gaussian in time with a full width at half maximum (FWHM) of 1.2 ps. Furthermore, we consider the spatial absorption profile of pump laser light. We solve the problem using a finite difference method.

The three-temperature simulation yields good agreement with TDTR measurements on Sample I at time delays between 100 and 1000 ps. Figure 4 (a) depicts the time-evolution of the temperatures $T_\uparrow$, $T_\downarrow$, and T_p computed for the center of the upmost Co layer (lines) together with TDTR data scaled to the simulation at a time delay of 300 ps (symbols). The dominant contribution to the thermoreflectance signal comes from the phonon temperature. It takes $\sim$ 200 ps until changes in the temperature within the optical penetration depth are small compared to the average temperature rise. Therefore, predicted and measured thermal response deviate from each other at shorter time delays. Due to the small value of g_ep in Cu[14], it takes $\sim$ 10 ps until the Cu layers thermalize with the Co layers via phonon thermal transport, resulting in an enhanced TDTR signal below $\sim$ 10 ps. Deviations at time delays longer than $\sim$ 1 ns originate from changes in the pump beam diameter with time delay that affected the thermal response measured but were not considered in the model.

Interestingly, the three-temperature model predicts SHA in both AP and P configurations [see Fig. 5]. During laser excitation, the $\uparrow$ electron reservoir gains a higher temperature than the $\downarrow$ electron reservoir, due to the assumption of $g_{\uparrow p} < g_{\downarrow p}$[16]. After the heating pulse, this initial SHA is rapidly transfered to the phonon reservoir via electron-phonon scattering. To understand the subsequent dynamic of the three temperatures in the P configuration, it is useful to define electron-phonon conductances per unit area in the Co layers, $G_{\uparrow\mathrm{p}} = g_{\uparrow\mathrm{p}} h_\mathrm{Co}$, and $G_{\downarrow\mathrm{p}} = g_{\downarrow\mathrm{p}} h_\mathrm{Co}$, where $h_\mathrm{Co} = 3$ nm is the thickness of each Co layer. We compare these electron-phonon conductances with the interface thermal conductances $G_\uparrow^\mathrm{Co/Cu}$ and $G_\downarrow^\mathrm{Co/Cu}$. For the parameter set chosen, $G_{\downarrow\mathrm{p}} \sim G_\downarrow^\mathrm{Co/Cu}$, while $G_{\uparrow\mathrm{p}} \ll G_\uparrow^\mathrm{Co/Cu}$. This means that in P configuration, heat is transported across a Co/Cu interface via the $\uparrow$ electron heat channel, before $\uparrow$ electrons thermalize with phonons in the Co layer. As a consequence, $T_\uparrow < T_\downarrow$ in the upper Co layers in the time delay range between $\sim$ 2 and $\sim$ 100 ps. This transient SHA develops throughout the multilayer and changes sign at a certain depth of the multilayer

that depends on the time delay. The profiles of $T_\uparrow$, $T_\downarrow$, and T_p predicted in AP and P configuration through a part of the Co/Cu multilayer are shown in Fig. 4 (b) and (c).

V. CONCLUSION

We introduced a three-temperature model capable of predicting the time-evolution of $T_\uparrow$, $T_\downarrow$, and T_p subsequent to pulsed laser heating. We used this model to quantify spin heat relaxation lengths in Co and in Cu, which justified the prediction of GMTR in our samples based on the W-F law. We measured the cross-plane thermal conductivity and the CPP-GMTR of Co/Cu multilayers. The experimental results are in very good agreement with the predictions based on the W-F law, indicating that the spin asymmetry coefficients do not change significantly with temperature. We found that TDTR measurements on Co/Cu multilayers are well explained by the three-temperature model. In contrast to the steady-state, the three-temperature model predicts SHA in the P configuration of the multilayer for a time-period of the order of 100 ps after pulsed laser heating.

Acknowledgments

This work was carried out in part in the Frederick Seitz Materials Research Laboratory Central Research Facilities, University of Illinois. Financial supports by the Army Research Office under Contract No. W911NF-14-1-0016 and by the German Research Foundation under DFG-Grant No. KI 1893/1-1 are kindly acknowledged.

Appendix A: Spin heat accumulation in steady-state

In Ref. 11, Valet and Fert derived the spin-diffusion equation from a Boltzmann equation and solved the problem of spin-dependent charge transport through a periodic Co/Cu multilayer. In the following, we assume that the constitutive equations for describing spin dependent thermal transport are equivalent to the constitutive equations for spin dependent charge transport[12] and discuss the thermal equivalent of the Valet and Fert model.

In steady-state,

$$J = J_\uparrow + J_\downarrow \equiv J_0 = \text{const.}, \tag{A1}$$

where J denotes heat current density. Differentiation of J in combination with the Fourier law yields (compare Eq. (17) in Ref. 11)

$$\frac{\partial^2(\Lambda_\uparrow T_\uparrow + \Lambda_\downarrow T_\downarrow)}{\partial z^2} = 0, \tag{A2}$$

where Λ denotes thermal conductivity.

The general solution of the spin heat diffusion equation, Eq. (1), and Eq. (A2) in a ferromagnetic metal (F) is given by

$$T_\uparrow - T_\downarrow = A\exp\left(\frac{z}{l_{\rm qF}}\right) + B\exp\left(\frac{-z}{l_{\rm qF}}\right) \tag{A3}$$

and

$$\Lambda_\uparrow T_\uparrow + \Lambda_\downarrow T_\downarrow = Ez + F. \tag{A4}$$

Combining Eqs. (A3) and (A4) yields

$$T_\uparrow(z) = \frac{1-\beta}{2}\left[A\exp\left(\frac{z}{l_{\rm qF}}\right) + B\exp\left(-\frac{z}{l_{\rm qF}}\right)\right] + \frac{1-\beta^2}{\Lambda_{\rm F}^*}(Ez+F), \tag{A5}$$

$$J_\uparrow(z) = -\Lambda_\uparrow\frac{\partial T_\uparrow}{\partial z} = -\frac{\Lambda_{\rm F}^*}{4l_{\rm qF}}\left[A\exp\left(\frac{z}{l_{\rm qF}}\right) - B\exp\left(-\frac{z}{l_{\rm qF}}\right)\right] - \frac{1+\beta}{2}E, \tag{A6}$$

$$T_\downarrow(z) = -\frac{1+\beta}{2}\left[A\exp\left(\frac{z}{l_{\rm qF}}\right) + B\exp\left(-\frac{z}{l_{\rm qF}}\right)\right] + \frac{1-\beta^2}{\Lambda_{\rm F}^*}(Ez+F), \tag{A7}$$

$$J_\downarrow(z) = -\Lambda_\downarrow\frac{\partial T_\downarrow}{\partial z} = \frac{\Lambda_{\rm F}^*}{4l_{\rm qF}}\left[A\exp\left(\frac{z}{l_{\rm qF}}\right) - B\exp\left(-\frac{z}{l_{\rm qF}}\right)\right] - \frac{1-\beta}{2}E, \tag{A8}$$

where we used a spin asymmetry coefficient β defined by

$$\Lambda_\uparrow = \frac{\Lambda_{\rm F}^*}{2(1-\beta)}, \tag{A9}$$

$$\Lambda_\downarrow = \frac{\Lambda_{\rm F}^*}{2(1+\beta)}. \tag{A10}$$

In a normal metal (N), $\beta = 0$, i.e.,

$$\Lambda_\uparrow = \Lambda_\downarrow = \frac{\Lambda_{\rm N}}{2}, \tag{A11}$$

and $\Lambda_{\rm F}^*$ and $l_{\rm qF}$ in Eqs. (A5) through (A8) are replaced by $\Lambda_{\rm N}$ and $l_{\rm qN}$.

The spin averaged temperature is defined by

$$\begin{aligned} J &= J_\uparrow + J_\downarrow \\ \Leftrightarrow -\Lambda\frac{\partial T}{dz} &= -\Lambda_\uparrow\frac{\partial T_\uparrow}{dz} - \Lambda_\downarrow\frac{\partial T_\downarrow}{dz} \\ \Rightarrow T(z) &= \frac{\Lambda_\uparrow}{\Lambda}T_\uparrow + \frac{\Lambda_\downarrow}{\Lambda}T_\downarrow + C, \end{aligned} \tag{A12}$$

where the integration constant C can be set to zero, because $\lim_{z\to\infty} T = \frac{1}{2}(T_\uparrow + T_\downarrow)$. Inserting Eqs. (A6) and (A8) into Eq. (A1) determines

$$E = -J, \tag{A13}$$

Inserting Eqs. (A5) and (A7) into Eq. (A12) yields the spin averaged temperature as

$$T = \frac{1-\beta^2}{\Lambda_{\rm F}^*}(-J+F). \tag{A14}$$

1. Bilayer model

We consider a semi-infinite ferromagnetic metal (F) in contact with a semi-infinite normal metal (N) and assume only bulk spin-dependent scattering and transparent interfaces. Vanishing SHA for $z \to \pm\infty$ and continuity of the spin-dependent temperatures and heat current densities at the interface at $z = 0$ yields the following solution in the F layer ($z <= 0$).

$$T_\uparrow(z) = \frac{1-\beta}{\Lambda_{\rm F}^*} J \left[\frac{\beta \Lambda_{\rm F}^* l_{\rm qN} l_{\rm qF}}{\Lambda_{\rm N} l_{\rm qF} + \Lambda_{\rm F}^* l_{\rm qN}} \exp\left(\frac{z}{l_{\rm qF}}\right) - (1+\beta) z \right] + T_0, \tag{A15}$$

$$J_\uparrow(z) = \frac{1}{2} J \left[-\frac{\beta \Lambda_{\rm F}^* l_{\rm qN}}{\Lambda_{\rm N} l_{\rm qF} + \Lambda_{\rm F}^* l_{\rm qN}} \exp\left(\frac{z}{l_{\rm qF}}\right) + (1+\beta) \right], \tag{A16}$$

$$T_\downarrow(z) = -\frac{1+\beta}{\Lambda_{\rm F}^*} J \left[\frac{\beta \Lambda_{\rm F}^* l_{\rm qN} l_{\rm qF}}{\Lambda_{\rm N} l_{\rm qF} + \Lambda_{\rm F}^* l_{\rm qN}} \exp\left(\frac{z}{l_{\rm qF}}\right) + (1-\beta) z \right] + T_0, \tag{A17}$$

$$J_\downarrow(z) = \frac{1}{2} J \left[\frac{\beta \Lambda_{\rm F}^* l_{\rm qN}}{\Lambda_{\rm N} l_{\rm qF} + \Lambda_{\rm F}^* l_{\rm qN}} \exp\left(\frac{z}{l_{\rm qF}}\right) + (1-\beta) \right], \tag{A18}$$

where T_0 is the temperature in the F layer at $z = 0$. In the N layer, the corresponing solution reads ($z > 0$)

$$T_\uparrow(z) = \frac{1}{\Lambda_{\rm N}} J \left\{ \frac{\beta \Lambda_{\rm N} l_{\rm qF} l_{\rm qN}}{\Lambda_{\rm N} l_{\rm qF} + \Lambda_{\rm F}^* l_{\rm qN}} \left[\exp\left(-\frac{z}{l_{\rm qF}}\right) - \beta \right] - z \right\} + T_0, \tag{A19}$$

$$J_\uparrow(z) = \frac{1}{2} J \left[\frac{\beta \Lambda_{\rm N} l_{\rm qF}}{\Lambda_{\rm N} l_{\rm qF} + \Lambda_{\rm F}^* l_{\rm qN}} \exp\left(-\frac{z}{l_{\rm qN}}\right) + 1 \right], \tag{A20}$$

$$T_\downarrow(z) = \frac{1}{\Lambda_{\rm N}} J \left\{ -\frac{\beta \Lambda_{\rm N} l_{\rm qF} l_{\rm qN}}{\Lambda_{\rm N} l_{\rm qF} + \Lambda_{\rm F}^* l_{\rm qN}} \left[\exp\left(-\frac{z}{l_{\rm qF}}\right) + \beta \right] - z \right\} + T_0, \tag{A21}$$

$$J_\downarrow(z) = \frac{1}{2} J \left[-\frac{\beta \Lambda_{\rm N} l_{\rm qF}}{\Lambda_{\rm N} l_{\rm qF} + \Lambda_{\rm F}^* l_{\rm qN}} \exp\left(-\frac{z}{l_{\rm qN}}\right) + 1 \right]. \tag{A22}$$

$$\tag{A23}$$

2. Spin-dependent thermal diffusion model for a periodic multilayer

To treat the multilayer problem, we consider two spin heat channels with fixed spin directions: the '+' heat channel with spin direction parallel to the x-axis and the '−' heat channel with spin direction antiparallel to the x-axis. In the P configuration of the multilayer, the '+' heat channel is characterized by the transport properties of majority (↑) spin electrons, while the '−' heat channel is characterized by the transport properties of minority (↓) spin electrons. In the AP configuration, the spin character of each channel changes alternates through successive F layers. Since we are interested in periodic magnetic multilayers with a large number of repetitions of F/N bilayers, we consider two F/N bilayers (F1/N2/F3/N4) with periodic boundary conditions. As before, we consider only bulk spin-dependent scattering and assume transparent interfaces. In AP configuration, application of the boundary conditions determines the coefficients A_i, B_i, and F_i in Eqs. (A5) through (A8) for layers $i \in 1, 2, 3, 4$ as

$$A_1 = B_1 = -A_3 = -B_3 = \frac{-\beta J l_{\mathrm{qN}} l_{\mathrm{qF}} \sinh\left(\frac{h}{l_{\mathrm{qF}}}\right)}{\Lambda_{\mathrm{N}} l_{\mathrm{qF}} \sinh\left(\frac{h}{l_{\mathrm{qN}}}\right) \sinh\left(\frac{h}{l_{\mathrm{qF}}}\right) + \Lambda_{\mathrm{F}}^* l_{\mathrm{qN}} \cosh\left(\frac{h}{l_{\mathrm{qN}}}\right) \cosh\left(\frac{h}{l_{\mathrm{qF}}}\right)}, \tag{A24}$$

$$A_2 = -B_2 = A_4 = -B4 = \frac{\beta J l_{\mathrm{qN}} l_{\mathrm{qF}} \cosh\left(\frac{h}{l_{\mathrm{qN}}}\right)}{\Lambda_{\mathrm{N}} l_{\mathrm{qF}} \sinh\left(\frac{h}{l_{\mathrm{qN}}}\right) \sinh\left(\frac{h}{l_{\mathrm{qF}}}\right) + \Lambda_{\mathrm{F}}^* l_{\mathrm{qN}} \cosh\left(\frac{h}{l_{\mathrm{qN}}}\right) \cosh\left(\frac{h}{l_{\mathrm{qF}}}\right)}, \tag{A25}$$

$$F_2 = \frac{\Lambda_{\mathrm{F}}^*}{1-\beta^2}\left[\beta A_1 \cosh\left(\frac{h}{l_{\mathrm{qN}}}\right) - Jh\left(\frac{1-\beta^2}{\Lambda_{\mathrm{F}}^*} + \frac{1}{\Lambda_{\mathrm{N}}}\right)\right] + T_0 \frac{\Lambda_{\mathrm{F}}^*}{1-\beta^2}, \tag{A26}$$

$$F_3 = 2\Lambda_{\mathrm{N}}\left[\beta A_1 \cosh\left(\frac{h}{l_{\mathrm{qN}}}\right) - Jh\left(\frac{1-\beta^2}{\Lambda_{\mathrm{F}}^*} + \frac{1}{\Lambda_{\mathrm{N}}}\right)\right] + T_0 \Lambda_{\mathrm{N}}, \tag{A27}$$

$$F_4 = \frac{3\Lambda_{\mathrm{F}}^*}{1-\beta^2}\left[\beta A_1 \cosh\left(\frac{h}{l_{\mathrm{qN}}}\right) - Jh\left(\frac{1-\beta^2}{\Lambda_{\mathrm{F}}^*} + \frac{1}{\Lambda_{\mathrm{N}}}\right)\right] + T_0 \frac{\Lambda_{\mathrm{F}}^*}{1-\beta^2}, \tag{A28}$$

where $e = -1.602 \times 10^{-19}$ As is the charge of an electron, and $2h$ is the thickness of the individual layers, which we assume to be equally thick. Furthermore, we defined $T_1(z = 0) = F_1/\Lambda_{\mathrm{N}} \equiv T_0$.

In P configuration, we obtain

$$\widetilde{A}_1 = -\widetilde{B}_1 = \widetilde{A}_3 = -\widetilde{B}_3, = \frac{-\beta J l_{\mathrm{qN}} l_{\mathrm{qF}} \sinh\left(\frac{h}{l_{\mathrm{qF}}}\right)}{\Lambda_{\mathrm{N}} l_{\mathrm{qF}} \cosh\left(\frac{h}{l_{\mathrm{qN}}}\right) \sinh\left(\frac{h}{l_{\mathrm{qF}}}\right) + \Lambda_{\mathrm{F}}^* l_{\mathrm{qN}} \sinh\left(\frac{h}{l_{\mathrm{qN}}}\right) \cosh\left(\frac{h}{l_{\mathrm{qF}}}\right)}, \tag{A29}$$

$$\widetilde{A}_2 = -\widetilde{B}_2 = \widetilde{A}_4 = -\widetilde{B}_4 = \frac{\beta J l_{\mathrm{qN}} l_{\mathrm{qF}} \sinh\left(\frac{h}{l_{\mathrm{qN}}}\right)}{\Lambda_{\mathrm{N}} l_{\mathrm{qF}} \cosh\left(\frac{h}{l_{\mathrm{qN}}}\right) \sinh\left(\frac{h}{l_{\mathrm{qF}}}\right) + \Lambda_{\mathrm{F}}^* l_{\mathrm{qN}} \sinh\left(\frac{h}{l_{\mathrm{qN}}}\right) \cosh\left(\frac{h}{l_{\mathrm{qF}}}\right)}, \tag{A30}$$

$$\widetilde{F}_2 = \frac{\Lambda_{\mathrm{F}}^*}{1-\beta^2}\left[\beta \widetilde{A}_1 \sinh\left(\frac{h}{l_{\mathrm{qN}}}\right) - Jh\left(\frac{1-\beta^2}{\Lambda_{\mathrm{F}}^*} + \frac{1}{\Lambda_{\mathrm{N}}}\right)\right] + T_0 \frac{\Lambda_{\mathrm{F}}^*}{1-\beta^2}, \tag{A31}$$

$$\widetilde{F}_3 = 2\Lambda_{\mathrm{N}}\left[\beta \widetilde{A}_1 \sinh\left(\frac{h}{l_{\mathrm{qN}}}\right) - Jh\left(\frac{1-\beta^2}{\Lambda_{\mathrm{F}}^*} + \frac{1}{\Lambda_{\mathrm{N}}}\right)\right] + T_0 \Lambda_{\mathrm{N}}, \tag{A32}$$

$$\widetilde{F}_4 = \frac{3\Lambda_{\mathrm{F}}^*}{1-\beta^2}\left[\beta \widetilde{A}_1 \sinh\left(\frac{h}{l_{\mathrm{qN}}}\right) - Jh\left(\frac{1-\beta^2}{\Lambda_{\mathrm{F}}^*} + \frac{1}{\Lambda_{\mathrm{N}}}\right)\right] + T_0 \frac{\Lambda_{\mathrm{F}}^*}{1-\beta^2}. \tag{A33}$$

The thermal resistance area products AW_{AP} and AW_{P} of one bilayer of the multilayer are given by

$$AW_{\mathrm{AP}} = -\frac{T_3(-b) - T_1(-b)}{J} = -\frac{F_3 - T_0\Lambda_{\mathrm{N}}}{\Lambda_N^* J}, \tag{A34}$$

$$AW_{\mathrm{P}} = -\frac{\widetilde{T}_3(-b) - \widetilde{T}_1(-b)}{J} = -\frac{\widetilde{F}_3 - T_0\Lambda_{\mathrm{N}}}{\Lambda_N^* J}. \tag{A35}$$

In the limit $h \ll \{l_{\mathrm{qN}}, l_{\mathrm{qF}}\}$, we obtain in first order in $\frac{h}{l_{\mathrm{qN}}}$ and $\frac{h}{l_{\mathrm{qF}}}$

$$AW_{\mathrm{AP}} = 2h\left(\frac{1}{\Lambda_{\mathrm{N}}} + \frac{1}{\Lambda_{\mathrm{F}}^*}\right) \equiv AW_{\mathrm{AP}}^{\mathrm{2CSR}}, \tag{A36}$$

$$AW_{\mathrm{P}} = 2h\left[\frac{1}{\Lambda_{\mathrm{N}}} + \frac{1}{\Lambda_{\mathrm{F}}^*} - \frac{\beta^2\Lambda_{\mathrm{N}}}{\Lambda_{\mathrm{F}}^*(\Lambda_{\mathrm{N}} + \Lambda_{\mathrm{F}}^*)}\right] \equiv AW_{\mathrm{P}}^{\mathrm{2CSR}}. \tag{A37}$$

Equations (A36) and (A37) are equal to the corresponding bilayer thermal resistance area products derived from a simpe two-current series resistor (2CSR) model that assumes parallel thermal transport through uncoupled spin channels (compare Ref. 11). Figure 6 shows AW_{AP} and AW_{P} as a functions of the spin heat relaxation length l_{qN}.

Appendix B: TDTR analysis using superposition of bidirectional heat flow

As discussed in Sec. III B, we use the superposition of individual solutions of a bidirectional heat flow model to analyze the TDTR measurements. Figure 7 (a) shows the individual solutions of the bidirectional heat flow model as blue solid lines. The different

curves correspond to different depths $z \in \{2, 6, 10, ..., 50\}$ nm of the heat flux boundary condition used for modeling the absorption of laser light. The superposition of the individual solutions weighted by the absorption profile is shown as black solid line. We approximated the absorption profile using an optical transfer matrix model. Optical constants, summarized in Table III, were determined using ellipsometry.

The thermalization length between electrons and phonons in Co is given by the spin heat relaxation lengths $l_{\mathrm{q1}} \approx 27$ nm and $l_{\mathrm{q2}} \approx 7$ nm [compare Secs. II B and II C]. As shown in Fig. 7 (a), at time delays longer than approximately 200 ps, the individual solutions for heat flux boundary conditions at depths below ~ 14 nm are close together indicating that the model is robust against changes of the absorption profile due to diffusion of hot electrons.

Appendix C: Parameter set of the three-temperature model of Sample I

Below, we discuss the parameter set considered for the simulation of TDTR measuremnets on Sample I using the three-temperature model. The values are listed in Table IV.

1. Interface thermal conductances $G_\uparrow$, $G_\downarrow$, and G_{p}

Pratt and Bass measured resistance area products AR of various metal$_1$/metal$_2$ interfaces[27]. For Ru/Co interfaces, they obtained $AR \approx 0.5$ fΩm^2. For Co/Cu interfaces, Pratt and Bass obtained $AR^* = (AR_\uparrow - AR_\downarrow)/4 \approx 0.5$ fΩm^2. We use the Wiedemann-Franz law to estimate the corresponding interface thermal conductances[26]. To obtain $G_\uparrow = G^*_{\mathrm{Co/Cu}}/[2(1-\gamma)]$ and $G_\downarrow = G^*_{\mathrm{Co/Cu}}/[2(1+\gamma)]$, we assume $\gamma = 0.77$ as discussed in Sec. II C.

For phonons, we consider a typical interface thermal conductance of 300×10^6 W m^{-2} K^{-1} at all interfaces, which is much smaller than the interace thermal conductances of electrons. Therefore, contribution of phonons to the total thermal conductivity is small.

2. Coupling parameters $g_{\uparrow\mathrm{p}}$, $g_{\downarrow\mathrm{p}}$, and $g_{\uparrow\downarrow}$

Definition of $g_{\uparrow\mathrm{p}}$ and $g_{\downarrow\mathrm{p}}$ of Co and of g_{ep} of Cu is discussed in Sec. II B. We estimated g_{ep} of Ru using g_{ep} of Pt measured in Ref. 15. Since at room temperature, electron-phonon

scattering dominates over spin-flip scattering, we assume that $g_{ee} \ll g_{ep}$. Based on this assumption, the three-temperature model is insensitive to g_{ee}. Therefore, we chose an arbitrary value in agreement with this assumption.

3. Thermal conductivities $\Lambda_\uparrow$, $\Lambda_\downarrow$, and Λ_p

Definition of $\Lambda_\uparrow$ and $\Lambda_\downarrow$ of Co and of Λ_e of Cu is discussed in Sec. II B. Since the thermal conductance of phonons in the Co/Cu multilayer is dominated by the Co/Cu interface thermal conductance, the model is insensitive to Λ_p. Therefore, we set Λ_p to the same arbitrary but small value for all layers.

4. Volumetric heat capacities $C_\uparrow$, $C_\downarrow$, and C_p

The thermalization time of electrons and phonons in the Co layers is much shorter than the duration of the laser pulse, i.e., only a small amount of the energy of the laser pulse is stored in the electron reservoir after the pulse[28]. This means that the sensitivity of the three-temperature model to the electronic heat capacity $C_e = C_\uparrow + C_\downarrow$ is negligibly small. The values of C_e were calculated using the low-temperature approximation $C_e = \pi^2 k_B^2 N(E_F) T/3$[29], where $N(E_F)$ is the density of electronic states at the Fermi Energy E_F, k_B is the Boltzmann constant, and T denotes temperature. In Co, $N_\downarrow(E_F) > N_\uparrow(E_F)$. We considered a spin dependence of $N(E_F)$ in Co that has been calculated using the density functional theory program WIEN2k[30].

Values for C_p were determined by substracting C_e from the respective total heat capacities taken from Ref. 31.

5. Absorption rates $P_\uparrow$ and $P_\downarrow$

The thermal response of the sample is linear in both the pump and probe powers. Therefore, accurate knowledge of the absorbed energy is not required for analyzing TDTR data. However, in the three temperature model, $P_\uparrow$, $P_\downarrow$, $g_{\uparrow p}$, and $g_{\downarrow p}$ determine the initial SHA

during laser excitation.

---

* Electronic address: kimling@illinois.edu

[1] M. N. Baibich, J. M. Broto, A. Fert, F. N. Van Dau, F. Petroff, P. Etienne, G. Creuzet, A. Friederich, and J. Chazelas, Phys. Rev. Lett. **61**, 2472 (1988), URL http://link.aps.org/doi/10.1103/PhysRevLett.61.2472.

[2] G. Binasch, P. Grünberg, F. Saurenbach, and W. Zinn, Phys. Rev. B **39**, 4828 (1989), URL http://link.aps.org/doi/10.1103/PhysRevB.39.4828.

[3] H. Sato, H. Henmi, Y. Kobayashi, Y. Aoki, H. Yamamoto, T. Shinjo, and V. Sechovsky, J. Appl. Phys. **76**, 6919 (1994), URL http://link.aip.org/link/?JAP/76/6919/1.

[4] J. Shi, K. Pettit, E. Kita, S. Parkin, R. Nakatani, and M. Salamon, Phys. Rev. B **54**, 15273 (1996), URL http://link.aps.org/doi/10.1103/PhysRevB.54.15273.

[5] G. E. W. Bauer, E. Saitoh, and B. J. van Wees, Nature Mater. **11**, 391 (2012), ISSN 1476-1122, URL http://dx.doi.org/10.1038/nmat3301.

[6] T. T. Heikkilä, M. Hatami, and G. E. W. Bauer, Phys. Rev. B **81**, 100408(R) (2010).

[7] F. K. Dejene, J. Flipse, G. E. W. Bauer, and B. J. van Wees, Nature Phys. **9**, 636 (2013), ISSN 1745-2473, URL http://dx.doi.org/10.1038/nphys2743.

[8] I. J. Vera-Marun, B. J. van Wees, and R. Jansen, Phys. Rev. Lett. **112**, 056602 (2014), URL http://link.aps.org/doi/10.1103/PhysRevLett.112.056602.

[9] R. L. Stamps, S. Breitkreutz, J. kerman, A. V. Chumak, Y. Otani, G. E. W. Bauer, J.-U. Thiele, M. Bowen, S. A. Majetich, M. Kläui, et al., J. Phys. D: Appl. Phys. **47**, 333001 (2014), URL http://stacks.iop.org/0022-3727/47/i=33/a=333001.

[10] M. Johnson and R. H. Silsbee, Phys. Rev. B **37**, 5312 (1988), URL http://link.aps.org/doi/10.1103/PhysRevB.37.5312.

[11] T. Valet and A. Fert, Phys. Rev. B **48**, 7099 (1993).

[12] A. Slachter, F. L. Bakker, and B. J. van Wees, Phys. Rev. B **84**, 174408 (2011), URL http://link.aps.org/doi/10.1103/PhysRevB.84.174408.

[13] J. Bass and W. P. Pratt Jr., J. Magn. Magn. Mater. **200**, 274 (1999).

[14] W. Wang and D. G. Cahill, Phys. Rev. Lett. **109**, 175503 (2012), URL http://link.aps.org/doi/10.1103/PhysRevLett.109.175503.

[15] G.-M. Choi, B.-C. Min, K.-J. Lee, and D. G. Cahill, submitted for publication (2015).

[16] M. J. Verstraete, J. Phys.: Condens. Matter **25**, 136001 (2013), URL http://stacks.iop.org/0953-8984/25/i=13/a=136001.

[17] D. G. Cahill, K. Goodson, and A. Majumdar, J. Heat Transfer **124**, 223 (2001).

[18] D. G. Cahill, Rev. Sci. Instrum. **75**, 5119 (2004).

[19] K. Kang, Y. K. Koh, C. Chiritescu, X. Zheng, and D. G. Cahill, Rev. Sci. Instrum. **79**, 114901 (2008).

[20] D. G. Cahill, P. V. Braun, G. Chen, D. R. Clarke, S. Fan, K. E. Goodson, P. Keblinski, W. P. King, G. D. Mahan, A. Majumdar, et al., Appl. Phys. Rev. **1**, 011305 (2014), URL http://scitation.aip.org/content/aip/journal/apr2/1/1/10.1063/1.4832615.

[21] R. Costescu, M. Wall, and D. Cahill, Phys. Rev. B **67**, 054302 (2003), URL http://link.aps.org/doi/10.1103/PhysRevB.67.054302.

[22] J. P. Feser and D. G. Cahill, Rev. Sci. Instrum. **83**, 104901 (2012).

[23] G.-M. Choi, R. B. Wilson, and D. G. Cahill, Phys. Rev. B **89**, 064307 (2014), URL http://link.aps.org/doi/10.1103/PhysRevB.89.064307.

[24] J. C. Jacquet and T. Valet, MRS Proceedings 12/1994; 384. DOI: 10.1557/PROC-384-477 **384**, 477 (1995).

[25] J. Kimling, K. Nielsch, K. Rott, and G. Reiss, Phys. Rev. B **87**, 134406 (2013), URL http://link.aps.org/doi/10.1103/PhysRevB.87.134406.

[26] R. B. Wilson and D. G. Cahill, Phys. Rev. Lett. **108**, 255901 (2012), URL http://link.aps.org/doi/10.1103/PhysRevLett.108.255901.

[27] W. P. Pratt Jr. and J. Bass, Appl. Surf. Sci. **256**, 399 (2009).

[28] J. Kimling, J. Kimling, R. B. Wilson, B. Hebler, M. Albrecht, and D. G. Cahill, Phys. Rev. B **90**, 224408 (2014), URL http://link.aps.org/doi/10.1103/PhysRevB.90.224408.

[29] Z. Lin, L. V. Zhigilei, and V. Celli, Phys. Rev. B **77**, 075133 (2008).

[30] pp. Taken from website: http://lamp.tu–graz.ac.at/ hadley/ss1/materials/dos/cobalt.html (Jan. 2015).

[31] Y. S. Touloukian and E. H. Buyco, *Thermophysical Properties of Matter - The TPRC Data Series - Volume 4 - Specific Heat - Metallic Elements and Alloys* (IFI/Plenum, 1971).

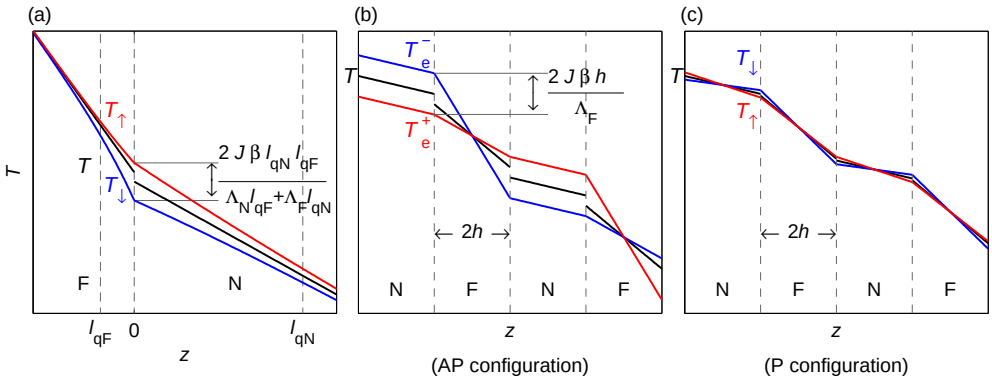

FIG. 1: (Color online). Simulation of spin heat accumulation (SHA) in steady-state assuming spin-dependent thermal conductivities in F layers and transparent interfaces. (a) SHA near the interface of a semi-infinite F layer in contact with a semi-infinite N layer. SHA at the F/N interface is proportional to the heat current density J and rises with increasing spin-asymmetry coefficient β and increasing spin heat relaxation lengths l_{qF} and l_{qN}. (b) and (c) SHA through a periodic F/N multilayer assuming $l_{\mathrm{qF}} = 5h$ and $l_{\mathrm{qN}} = 50h$. In AP configuration (b), SHA in N layers is proportional to $J\beta$. In P configuration (c), SHA is negligible. The difference in the temperature drops of the two configurations reveals the CPP-GMTR effect.

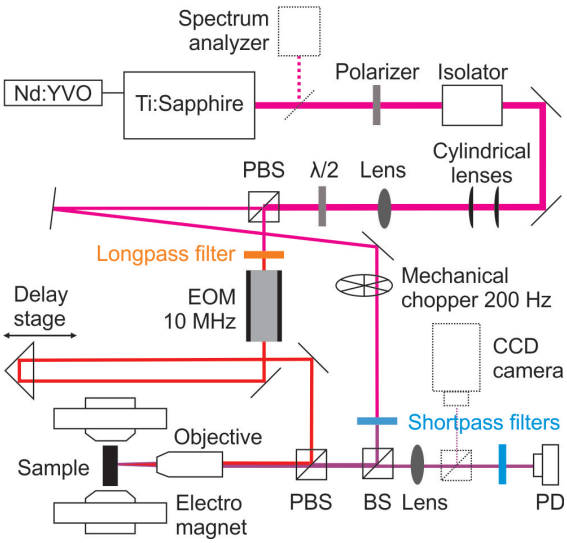

FIG. 2: (Color online) Scheme of the time-domain thermoreflectance setup described in the main text. PBS: polarizing beam splitter, EOM: electro optic modulator, BS: beam splitter, PD: photodiode.

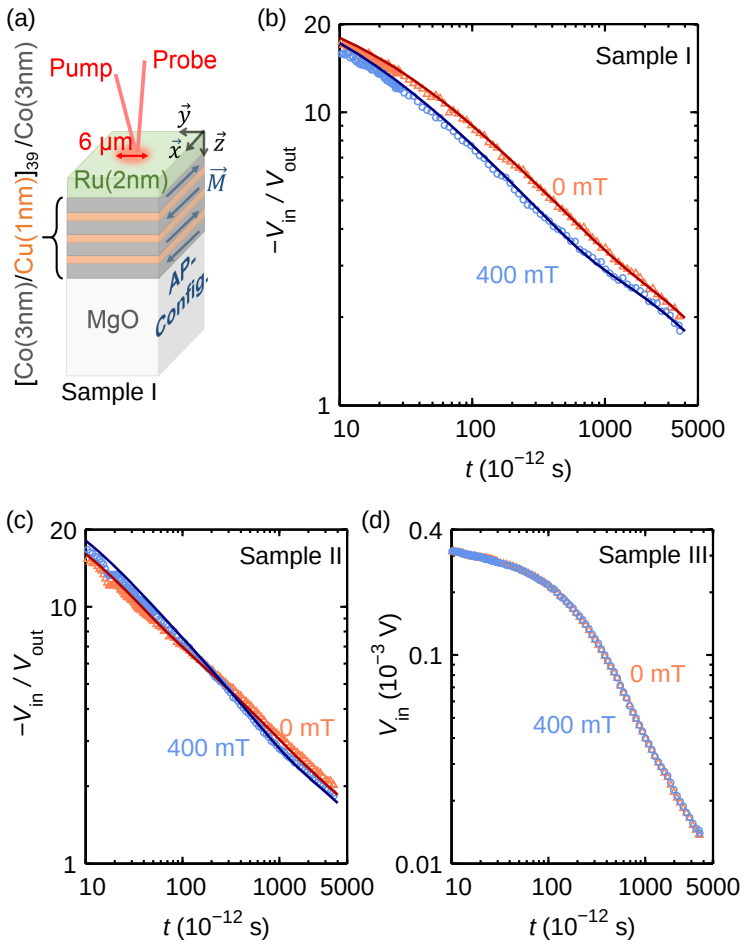

FIG. 3: (Color online). (a) Scematic of Sample I in AP configuration studied using time-domain thermoreflectance (TDTR). (b) TDTR data (symbols) recorded on Sample I at zero applied field (AP config.) and in an in-plane field of 400 mT (P config.). The ratio of in-phase and out-of-phase voltages, $-V_{\rm in}/V_{\rm out}$, mimics the thermal response of the sample. The best fits between predicted and measured thermal response (shown as solid lines) yield cross-plane thermal conductivities $\Lambda_{\rm AP} = 18 \pm 2$ and $\Lambda_{\rm P} = 32 \pm 3$ W m^{-1} K^{-1}. (c) Corresponding curves for Sample II yielding $\Lambda_{\rm AP} = 17 \pm 1$ and $\Lambda_{\rm P} = 28 \pm 5$ W m^{-1} K^{-1}. (d) $V_{\rm in}$ as a function of time delay measured on Sample III.

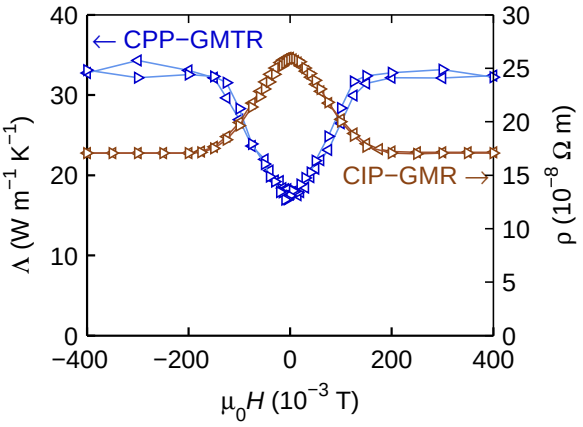

FIG. 4: (Color online). Cross-plane thermal conductivity Λ (left y-axis) and in-plane electrical resistivity ρ (right y-axis) measured on Sample I as a function of magnetic flux density $\mu_0 H$. Left- and right-pointing triangles indicate the direction of the field sweep. Lines serve as a guide to the eye.

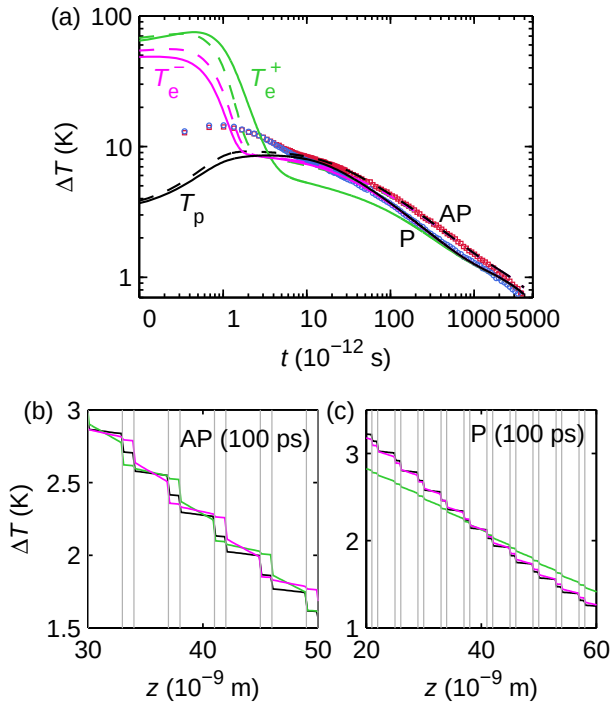

FIG. 5: (Color online). Three-temperature simulation of pulsed laser heating of Sample I. (a) Temperatures of majority-spin electrons ($T_\uparrow$), minority-spin electrons ($T_\downarrow$), and phonons (T_p) in the center of the upmost Co layer of Sample I in AP (solid lines) and P (dashed lines) configuration. The model succeeds in explaining the experimental data (symbols) over a wide range of time delays t. (b) and (c) Temperature profiles in AP and P configuration at time delay of 100 ps. In AP configuration, the sign of SHA in the Cu layers alternates. In contrast to steady-state, the three-temperature model predicts SHA in both AP and P configurations.

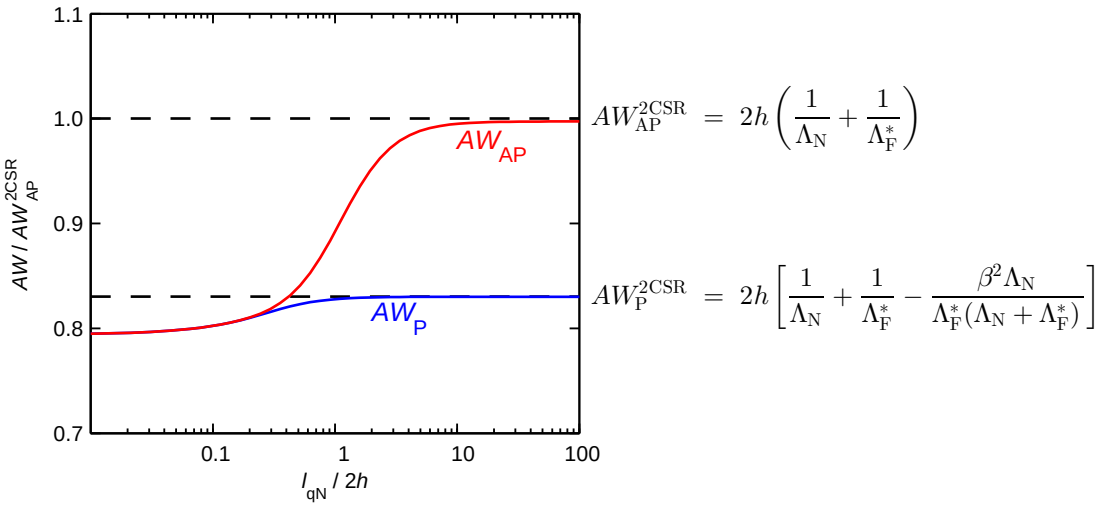

FIG. 6: (Color online). Thermal resistance area product AW of one bilayer of a periodic multilayer as function of the spin heat relaxation length l_{qN} of the normal metal layers in the antiparallel (AW_{AP}, red line) and the parallel (AW_{P}, blue line) magnetic configuration. In the limit $l_{\mathrm{qN}}/h \gg 1$, AW_{AP} and AW_{P} converge to the respective thermal resistance area products determined from a simplified two-current series resistor (2CSR) model that assumes parallel thermal transport through uncoupled spin channels [Eqs. (A36) and (A37)].

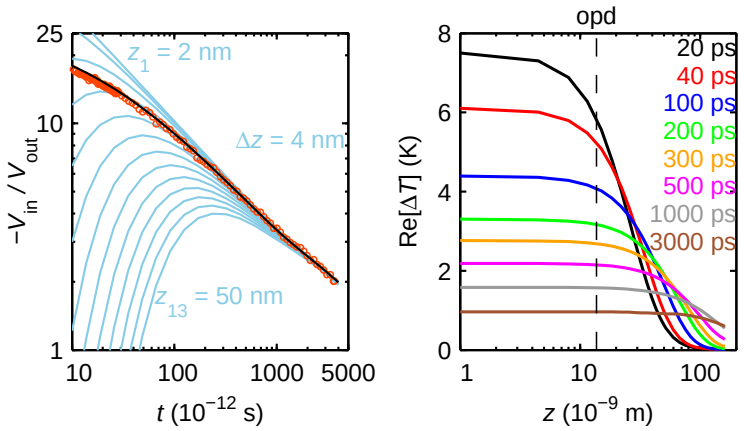

FIG. 7: (Color online). (a) TDTR ratio $-V_{\rm in}/V_{\rm out}$ of Sample I in AP configuration. Red circles: measurement data. Light blue lines: solutions from a bidirectional thermal diffusion model with heat flux boundary condition at different depths $z_{\rm i}$ from the surface as indicated in the figure. Black line: superposition of the solutions of the bidirectional model, weighted by the absorption profile. (b) Corresponding Temperature profiles through Sample I at time delays indicated in the graph. The verical dashed line indicates the optical penetration depth (opd).

TABLE I: Properties of sample I. Λ: thermal conductivity, C: volumetric heat capacity, h: layer thickness, G: interface thermal conductance.

	Λ	C	h
	(W m^{-1} K^{-1})	(10^6 J m^{-3} K^{-1})	(10^{-9} m)
Co/Cu ML	32±3[a] (P); 18±2[a] (AP)	3.64[b]	161±3[c]
MgO	40[a]	3.36[d]	∞
$G_{\mathrm{Co/MgO}} = (300 \pm 27) \times 10^6$ W m^{-2} K^{-1} [a]			

[a]Determined from TDTR measurements.

[b]Average value using volumetric heat capacities of Co and of Cu taken from Reference 31.

[c]Nominal total thickness of Ru(2nm)/[Co(3nm)/Cu(1nm)]$_{39}$Co(3nm) multilayer, confirmed using x-ray reflectometry.

[d]Reference 31.

TABLE II: Properties of sample II. Λ: thermal conductivity, C: volumetric heat capacity, h: layer thickness, G: interface thermal conductance.

	Λ (W m^{-1} K^{-1})	C (10^6 J m^{-3} K^{-1})	h (10^{-9} m)
Ru	45±5[a]	2.90[b]	57±2[c]
Co/Cu ML	28±5[d] (P); 17±1[d] (AP)	3.64[e]	159±3[f]
MgO	40[d]	3.36[b]	∞
$G_{\mathrm{Ru/Co}} = 1400 \times 10^6$ W m^{-2} K^{-1} [g]			
$G_{\mathrm{Co/MgO}} = 328 \times 10^6$ W m^{-2} K^{-1} [h]			

[a]Determined from electrical sheet resistance measurements and the Wiedemann-Franz law.

[b]Reference 31.

[c]Determined using picosecond acoustics.

[d]Determined from TDTR measurements.

[e]Average value using volumetric heat capacities of Co and of Cu taken from Reference 31.

[f]Nominal total thickness of Ru(2nm)/[Co(3nm)/Cu(1nm)]$_{39}$Co(3nm) multilayer, confirmed for Sample I using x-ray reflectometry.

[g]Estimated using experimentally determined values of the interface resistance between Ru and Co and the Wiedemann-Franz law[26,27]

TABLE III: Refractive index n and extinction coefficient k determined using ellipsometry.

	n	k
Ru[a]	5.3	4.9
Co/Cu ML[b]	3.2	4.7

[a]Reference sample: Ru(60nm) on MgO
[b]Sample I

TABLE IV: (Color online). Parameter set used for the three-temperature model of Sample I in AP configuration. Λ: thermal conductivity, C: volumetric heat capacity, h: layer thickness, G: interface thermal conductance. Subscript p refers to phonons, superscripts + and − distinguish the two electron heat channels of opposite spin direction. Properties of majority spin electron electrons are indicated in italics and red font color, properties of minority spin electrons are indicated in blue font color.

	Λ_+	Λ_-	Λ_p	C_+	C_-	C_p	$g_{+\mathrm{p}}$	$g_{-\mathrm{p}}$	g_{+-}	h	G_+	G_-	G_p
	(W m^{-1} K^{-1})			(10^4 J m^{-3} K^{-1})			(10^{17} W m^{-3} K^{-1})			(10^{-9} m)	(10^9 W m^{-2} K^{-1})		
Ru	18	18	5	3	3	284	2.3	2.3	0.1	2	7	7	0.3
Co	*44*	16	5	*1*	10	361	*0.6*	3.9	0.1	3	*31*	4	0.3
Cu	75	75	5	2	2	339	0.4	0.4	0.1	1	4	*31*	0.3
Co	16	*44*	5	10	*1*	361	3.9	*0.6*	0.1	3	*31*	4	0.3
Cu	75	75	5	2	2	339	0.4	0.4	0.1	1	4	31	0.3
MgO	0	0	40	0	0	336	0	0	0	∞	-	-	-